International Journal of Engineering Science 48 (2010) 1681–1691

Contents lists available at ScienceDirect

International Journal of Engineering Science

journal homepage: www.elsevier.com/locate/ijengsci

Estimation of red blood cell volume fraction from overall permittivity measurements

T.I. Zohdi [a,b,*], F.A. Kuypers [b], W.C. Lee [a,b]

[a] Department of Mechanical Engineering, 6195 Etcheverry Hall, University of California, Berkeley, CA 94720-1740, USA
[b] Children's Hospital Oakland Research Institute (CHORI), Oakland, CA, USA

ARTICLE INFO

Article history:
Available online 8 June 2010

Keywords:
Effective electromagnetic properties
Red blood cells
Volume fraction estimate

ABSTRACT

The rapid testing of red blood cell (RBC) volume fraction ("hematocrit") is becoming increasingly important to identify blood disorders ("hemoglobinopathies"). Electromagnetic techniques provide an advantageous way to measure blood properties, primarily because they are inexpensive, quick and noninvasive. The goal of this paper is to develop estimates of the RBC volume fraction levels of whole blood from macroscopic electromagnetic (permittivity) measurements. The approach taken is to generate volume fraction estimates by inverting classical bounds on the effective permittivity of dielectric mixtures. The usefulness of the approach is that, given the permittivities of the plasma (known), cells (known) and whole mixture (measured), one can determine the cell volume fraction and compare it to the levels found in healthy blood. The deviation of the properties can be used to help characterize certain blood disorders. The expressions developed are not limited to RBC measurement, and are applicable to any cell-in-solution system. Through correlation of our laboratory measurements, the analytical expressions and direct large-scale numerical simulations, the results suggest that RBCs form high-permittivity cell-networks by making cell-to-cell contact, even at relatively low volume fraction.

1. Introduction

1.1. General background

Red blood cells (RBCs), which are responsible for the transport of oxygen and carbon dioxide, are the most prevalent type of cells in human blood. The average cellular volume of each cell (82–96 femtoliters) is occupied by a high concentration of the oxygen carrying protein hemoglobin at a concentration of 30–36%. The lifespan of the human RBCs is approximately 120 days after they are released from the bone marrow as reticulocytes. Typically 4–6 million RBCs per cubic millimeter occupy 41–52% of blood volume (hematocrit). The typical bi-concaval shape of RBCs endows the cell with ideal deformability characteristics. This allows RBCs to efficiently perform their function in small capillaries. Alterations in RBC properties, including shape, volume and membrane characteristics will lead to a decreased lifespan and when not compensated by increased production, a lower volume and anemia. Genetic disorders in cytoskeletal proteins (the cell wall "scaffolding") results in RBC pathologies, such as hereditary spherocytosis and hereditary elliptocytosis [5,8,9]. Deviations in cytosolic and membrane proteins may affect the state of hydration of the cell and thereby its characteristics. Fig. 1 illustrates some examples of unhealthy cell morphologies. In normal blood in addition to discocytes, echinocytes and stomatocytes can be observed. Acanthocytes are observed in acquired hepatic syndromes, codocytes are

* Corresponding author at: Department of Mechanical Engineering, 6195 Etcheverry Hall, University of California, Berkeley, CA 94720-1740, USA.
E-mail address: zohdi@me.berkeley.edu (T.I. Zohdi).

0020-7225/$ - see front matter © 2010 Elsevier Ltd. All rights reserved.
doi:10.1016/j.ijengsci.2010.04.013

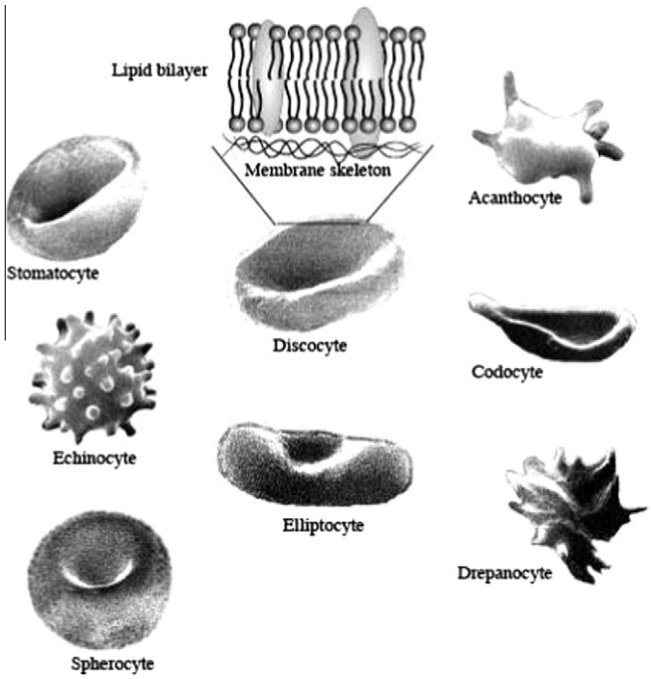

Fig. 1. The red blood cell membrane encloses the cytosol with hemoglobin. The membrane consists of a lipid bilayer which interacts with a spectrin skeleton giving the normal red blood cell its typical discocyte shape. The diameter of a healthy red blood cell (7.4–8.2 μm) can be markedly different in disease (2–11 μm) and can exhibit a variety of shapes. The drawings were created by F. Kuypers, based on the photographs of Bessis [1].

found in thalassemia. In sickle cell disease, hemoglobin polymers will distort the shape of the cell and drepanocytes are observed. Elliptocytes are the result of membrane disorders where interactions in the horizontal direction (e.g. spectrin–spectin interactions) are disrupted, and spherocytes are observed in membrane disorders where the interaction between the lipid bilayer and the underlying membrane skeleton is dysfunctional. The number of humans that are affected by sickle cell disease, thalassemia and other hemoglobinopathies, runs in the millions [7,18]. Such disorders lead to altered hemoglobin and result in changes in RBC properties, which is related to blood pathology, including anemia.

1.2. Objectives

The rapid testing of RBC data of individuals to define hematologic characteristics and possibly pathology is important. Quick and inexpensive electromagnetic measurements are considered to be an important technique to measure blood properties. The goal of this paper is to develop estimates of the volume fraction levels of cells in whole blood from a simple macroscopic electromagnetic measurement of the overall blood properties, at relatively low (nonoptical) frequencies (below one GHz). The approach taken here is to develop bounds on the possible volume fraction by inverting the classical bounds on the overall permittivity of electromagnetic mixtures. The usefulness of the approach is that given the permittivities of the buffer (representing the plasma, known), cell (known) and whole mixture (measured) one can determine the cell volume fraction. This information is useful to compare against the nominal volume fraction (hematocrit) values for healthy individuals.

Remark. In a previous report we described a rapid simulation of (high-frequency) light scattering by RBCs [24].

2. Laboratory experiments

The relative permittivity of RBC suspensions was measured at different volume fractions in the radio frequency (RF) range (0.3 MHz-1 GHz) using an open-ended coaxial line sensor technique [10]. The relative permittivity of RBC suspensions was corrected to compensate for electrode polarization effects, followed by curve-fitting which enabled extrapolations to calculate the static relative permittivity.

2.1. Preparation of human red blood cells (RBC)

Blood samples from healthy donors were collected in EDTA as anticoagulant, after informed consent, at the Children's Hospital Oakland Research Institute (CHORI). Whole blood was kept at 4 °C and used within 24 h after collection. RBCs were

isolated by centrifugation, plasma and the buffy coat were removed and the RBCs were washed three times in ten volumes of phosphate-buffered saline. The RBCs were re-suspended at approximately 30% volume fraction in phosphate buffered saline and stored at 4 °C until used within 48 h. The exact cell count in the suspension was determined using the ADIVA 120 hematology system, and the suspensions were diluted to the indicated volume fraction levels.

2.2. Experimental apparatus for permittivity measurements

We used an open-ended coaxial line sensor [10] made by an SMB jack (male) connector and an E5071B network analyzer (Agilent Technology). The network analyzer measured the sensor admittance, whose imaginary part represented the relative permittivity of a surrounding material at the sensor end. In order to standardize the sensor, we used two kinds of dielectric reference materials; air and deionized water. The air measurement corrected the RF phase offset between calibration and sensor planes. The deionized water measurement (relative permittivity of 78.3 [10]) was used as a reference value of the relative permittivity. After the sensor standardization, the relative permittivity of a buffer solution and RBC suspensions at indicated volume fractions were measured in the frequency range from 0.3 MHz to 1 GHz at 201 distinct values.

2.3. Correction for the electrode polarization effect

The relative permittivity values contained errors from the electrode polarization effect [16,17]. At RBC concentrations of up to 10% volume fraction the electrode polarization effect of RBC suspensions is the same as that of the buffer solution. In our experiments we diluted the RBC suspensions within a 2–10% range, as at higher concentrations, the electrode polarization effect shows complex and nonlinear behavior, that can only be characterized using special experimental methods (reviewed by Schwan [16]), and is beyond the present scope of this work. Fig. 2 shows the corrected relative permittivity of RBC suspensions with different concentration levels. Our measured permittivity data correlates well with previous reports [17].

2.4. Relative permittivity

In order to obtain the static relative permittivity, we used curve-fittings and extrapolations from the corrected relative permittivity with sigmoidal curve functions used by Schwan [17]. The solid lines in Fig. 2 are fitted curves from the measured values, and allowed *extrapolation to the static relative permittivity* from the curves. Fig. 2 shows the averages and standard deviations of the static relative permittivity from five repeated measurements.

3. Theoretical estimates: extraction of cell data from cell-in-solution measurements

Within a sample of material, a mixture of cells and buffer in the case of interest, the properties are characterized by a spatially variable permittivity $\boldsymbol{\epsilon}(\boldsymbol{x})$. Typically, in order to characterize the overall effective permittivity, a relation between averages is determined (Fig. 3)

$$\langle \boldsymbol{D} \rangle_{\Omega} = \boldsymbol{\epsilon}^{*} \cdot \langle \boldsymbol{E} \rangle_{\Omega}, \tag{3.1}$$

where $\langle \cdot \rangle_{\Omega} \stackrel{\text{def}}{=} \frac{1}{|\Omega|} \int_{\Omega} \cdot d\Omega$ is the averaging operator and $\boldsymbol{D}$ and $\boldsymbol{E}$ are the electrical flux and electric field within a statistically representative volume element (RVE) of volume $|\Omega|$. The permittivity tensor $\boldsymbol{\epsilon}^{*}$ represents the effective overall permittivity

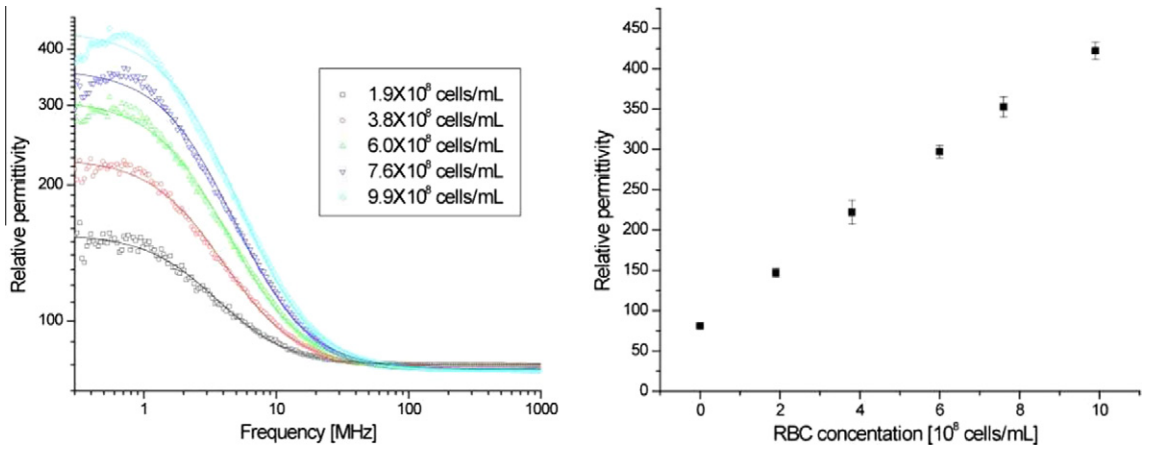

Fig. 2. Measured relative permittivity of RBC suspensions for different cell concentrations ($0.019 \leqslant v_2 \leqslant 0.099$), which directly correspond to volume fractions occupied by the cells: (a) Measured relative permittivity in the frequency range from 0.3 MHz to 1 GHz. Dots and solid lines represent measured data points and their fitted curves (solid lines on the left), respectively; (b) Static relative permittivity for different cell concentrations.

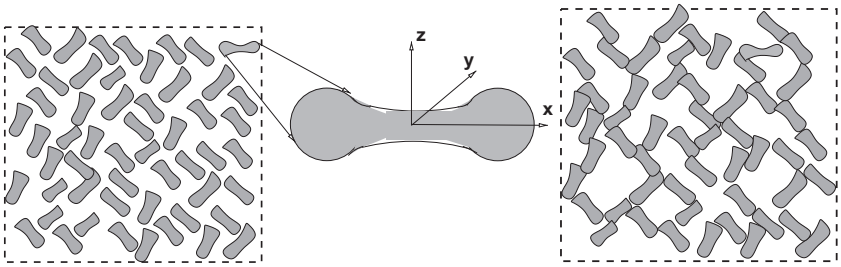

Fig. 3. LEFT: A representative volume element (RVE), with well-separated cells. RIGHT: An RVE with a chain-like network of cells for the same volume fraction as on the LEFT.

of the cell and buffer mixture. For a sample to be statistically representative, it must contain a reasonably large number of cells. If the effective response is assumed to be linear and isotropic (a mixture of randomly oriented cells) the relation between averages can be written as

$$\epsilon^* \stackrel{\text{def}}{=} \sqrt{\frac{\langle \boldsymbol{D}\rangle_\Omega \cdot \langle \boldsymbol{D}\rangle_\Omega}{\langle \boldsymbol{E}\rangle_\Omega \cdot \langle \boldsymbol{E}\rangle_\Omega}}, \tag{3.2}$$

where $\boldsymbol{\epsilon}^* = \epsilon^* \mathbf{1}$ and $\mathbf{1}$ is the identity tensor. Since we will be dealing with samples comprised of randomly dispersed cells in buffer, we shall assume an overall isotropic response, hence Eq. (3.2) is appropriate to describe the effective permittivity.

3.1. Effective permittivity estimates

Estimates on $\boldsymbol{\epsilon}^*$ as a function of the volume fraction and properties of the constituents have been developed over the last 150 years. For example, see works dating back to Maxwell [13,14] and Lord Rayleigh [15] (1892). There exist several other approaches which seek to estimate or bound the aggregate responses microheterogeneous materials. The most elementary set of estimates (which are rigorous bounds) to interpret for electrical permittivity are $\langle \boldsymbol{\epsilon}^{-1}(\boldsymbol{x})\rangle_\Omega^{-1} \leqslant \boldsymbol{\epsilon}^* \leqslant \langle \boldsymbol{\epsilon}(\boldsymbol{x})\rangle_\Omega$, where $\boldsymbol{\epsilon}(\boldsymbol{x})$ represents the spatially variable permittivity of the mixture and the upper bound is generated by assuming that the electric field is uniform (an approximation) throughout the medium and the lower bound is generated by assuming that the electric field flux is uniform (another approximation) throughout the medium. In the electromagnetics literature, the two-sided bounds are often referred to as the Wiener bounds [21]. These inequalities mean that the eigenvalues of the tensors $\boldsymbol{\epsilon}^* - \langle \boldsymbol{\epsilon}^{-1}\rangle_\Omega^{-1}$ and $\langle \boldsymbol{\epsilon}\rangle_\Omega - \boldsymbol{\epsilon}^*$ are non-negative. In the case of isotropy, the bounds may be written as

$$\left(\frac{v_2}{\epsilon_2} + \frac{1-v_2}{\epsilon_1}\right)^{-1} = \langle \epsilon^{-1}(\boldsymbol{x})\rangle_\Omega^{-1} \leqslant \epsilon^* \leqslant \langle \epsilon(\boldsymbol{x})\rangle_\Omega = v_2\epsilon_2 + (1-v_2)\epsilon_1, \tag{3.3}$$

where v_2 is the volume fraction of the cells (the volume fraction of the other phase is v_1, where $v_1 + v_2 = 1$), ϵ_2 is the permittivity of the cells and ϵ_1 is the permittivity of the surrounding buffer. Typically, the bounds are quite wide and provide only rough qualitative information. However, improved estimates have been developed, for example the well-known Hashin–Shtrikman bounds [11]

$$\left(\frac{v_2}{\epsilon_2} + \frac{1-v_2}{\epsilon_1}\right)^{-1} \leqslant \underbrace{\epsilon_1 + \frac{v_2}{\frac{1}{\epsilon_2-\epsilon_1} + \frac{1-v_2}{3\epsilon_1}}}_{\epsilon^{*,-}} \leqslant \epsilon^* \leqslant \underbrace{\epsilon_2 + \frac{1-v_2}{\frac{1}{\epsilon_1-\epsilon_2} + \frac{v_2}{3\epsilon_2}}}_{\epsilon^{*,+}} \leqslant v_2\epsilon_2 + (1-v_2)\epsilon_1. \tag{3.4}$$

Such bounds are the tightest possible on isotropic effective responses, with isotropic two phase microstructures, where only the volume fractions and phase contrasts of the constituents are known. Note that no further geometric information, such as the number and nature of cells, etc., contributes to these bounds. Generally, the upper bound is more accurate (closer to the actual effective property) for a microstructure comprised of a high-permittivity interstitial network/matrix (buffer) surrounding well-separated low-permittivity regions. If the cells touch one another, then the upper bound is quite accurate, since the cells form a high-permittivity network that separates low-permittivity buffer regions from one another (Fig. 3). We shall employ these bounds for the rest of the analysis, however, other methods could also be used. The lower bound is typically more accurate for microstructures where well-separated, high-permittivity, particles (cells) are surrounded by a lower permittivity matrix (buffer). Thus, the lower bound would be more accurate at extremely low volume fraction of cells; well below the levels tested in this paper. At very high volume fractions (also outside the scope of the present work), neither bound would dominate. A complete survey of the estimation of effective properties of heterogeneous materials, based on the properties of the constituents, is outside the scope of the present work. However, for a relatively survey and analysis of a variety of analytical approaches, see Torquato [19] and for computational approaches, see Zohdi and Wriggers [23].

3.2. Interpreting the measurements

After a series of algebraic manipulations, the Hashin–Shtrikman bounds for the permittivity may be inverted to solve for bounds on v_2

$$\underbrace{\frac{(\epsilon^* - \epsilon_1)3\epsilon_2}{(\epsilon^* + 2\epsilon_2)(\epsilon_1 - \epsilon_2)}}_{\stackrel{\text{def}}{=} v_2^-} \leqslant v_2 \leqslant \underbrace{\frac{(\epsilon^* - \epsilon_1)(2\epsilon_1 + \epsilon_2)}{(2\epsilon_1 + \epsilon^*)(\epsilon_2 - \epsilon_1)}}_{\stackrel{\text{def}}{=} v_2^+} \tag{3.5}$$

where inverting the upper bound Hashin–Shtrikman bound generates v_2^- and inverting the lower bound Hashin–Shtrikman bound generates v_2^+. The utility of this inversion is that given the permittivities of the buffer (known), cell (known) and whole mixture (measured) one can determine the cell volume fraction and compare it to the nominal response of a healthy group of cells. The relation in Eq. (3.5) is rather general, and can be used for any cell-in-solution system.

In order to illustrate how the inverted bounds may be used to aid in interpreting experiments, consider that the relative (to vacuum) permittivity of hemoglobin (or "cell-only") responses is approximately $\epsilon_2/\epsilon_0 \approx 6000$ (an estimate, since it is difficult to measure a "pure" interior cell material), while the buffer was $\epsilon_1/\epsilon_0 = 81.12$ (measured). With this information, and the overall response measurements made before one can generate the volume fraction bounds (Table 1). Recall, that the upper bound is quite accurate for touching cells, forming networks, which appears to be the present case. In order to provide a clear, continuous, calibration, we form a convex combination of the upper and lower bounds ($0 \leqslant \theta_v \leqslant 1$)

$$v_2 = \theta_v v_2^+ + (1 - \theta_v) v_2^-, \tag{3.6}$$

where, provided measurements are made for v_2 (as they have been made in this study), one can solve for the θ_v value, representing which bound (and microstructural morphology) is dominant

$$\theta_v = \frac{v_2 - v_2^-}{v_2^+ - v_2^-}. \tag{3.7}$$

Specifically,

- $\theta_v < 1/2$ indicates that v_2^- is dominant, which is generated by the Hashin–Shtrikman *upper* bound, where the effective response is indicative of cells touching, while
- $\theta_v > 1/2$ indicates that v_2^+ is dominant, which is generated by the Hashin–Shtrikman *lower* bound, where the effective response is indicative of well-separated cells.

The derived bounds on v_2 ($v_2^- \leqslant v_2 \leqslant v_2^+$) are general and hold for any combination of known values of ϵ_1, ϵ_2 and ϵ^*. For the case at hand, θ_v (Table 1) is comfortably less than 1/2 (the lower volume fraction bound being more accurate, generated by the Hashin–Shtrikman permittivity upper bound) leading to the hypothesis that the cells are touching and forming high-permittivity networks. Although the high-permittivity network effect is dominant at very low volume fractions, the effect is steadily less so with increasing volume fraction, characterized by an increasingly larger θ_v. Alternatively, one could directly relate the quality (narrowness) of the bounds on the permittivity to the measure value by writing ($0 \leqslant \theta_\epsilon \leqslant 1$)

$$\epsilon^* = \theta_\epsilon \epsilon^{*+} + (1 - \theta_\epsilon)\epsilon^{*-}, \tag{3.8}$$

where, provided measurements are made for ϵ^* (as they have been made in this study), one can solve for the θ_ϵ value, representing which bound (and microstructural morphology) is dominant

$$\theta_\epsilon = \frac{\epsilon^* - \epsilon^{*-}}{\epsilon^{*+} - \epsilon^{*-}}. \tag{3.9}$$

As with the θ_v metric (however, essentially reversed): (1) if $\theta_\epsilon > 1/2$, this indicates that ϵ^*+ is dominant, which is the Hashin–Shtrikman *upper* bound, where the effective response is indicative of by cells touching, while (2) if $\theta_\epsilon < 1/2$ this indicates that ϵ^*- is dominant, which is the Hashin–Shtrikman *lower* bound, where the effective response is indicative of well-separated

Table 1
The measured (relative permittivity, $\epsilon_i = \epsilon_{ri}\epsilon_o$, ϵ_o being the vacuum permittivity) response for radiation at 1 MHz. Volume fractions above 0.1 were difficult to measure because the polarization effect cannot be canceled at the higher volume fraction values. The relative permittivity of the buffer alone was measured to be $\epsilon_{r1} = 81.12$.

v_2	ϵ_r^*(measured mean)	v_2^-(from ϵ^*+)	v_2^+(from ϵ^*-)	θ_v(calculated)	$\epsilon_r^{*-}(v_2)$	$\epsilon_r^{*+}(v_2)$	θ_ϵ(calculated)
0.019	147.14	0.0177382	0.2348342	0.0058123	85.6437922	157.0738288	0.9289679
0.038	221.97	0.0350468	0.3816693	0.0085199	90.3389545	233.9887411	0.9163330
0.060	297.05	0.0534005	0.4894688	0.0151342	96.0026452	324.2729706	0.8807423
0.076	352.67	0.0668532	0.5490572	0.0189688	100.2838741	390.7757183	0.8688235
0.099	422.40	0.0835484	0.6077450	0.0294767	106.6929048	487.6406536	0.8287412

cells. This is alternative, yet equivalent representation of the cell-system behavior. As Table 1 indicates, θ_ϵ is comfortably larger than 1/2, again indicating that the Hashin–Shtrikman upper bound is dominant.

Remark. It is important to note that the hypothesized network connectivity of cells occurs at low volume fractions, as tested in our experiments, where the cell suspensions were continuously mixed to avoid cells from settling at the bottom of the test apparatus. We emphasize that, in the experiments, the mean values of different random realizations of cells were measured and recorded in the previous Fig. 2 and Table 1. It is important to emphasize that this connectivity is not a Rouleux formation ("coin stacking") arrangement which is sometimes observed at high volume fractions.

3.3. Observations

The correlation of the measurements and the analytical expressions (bounds) imply that RBCs form high-permittivity cell-networks by making cell-to-cell contact, even at low volume fractions. This observation is extremely important in order to make reliable estimates of volume fraction levels from overall cell-in-solution measurements. However, in order to strengthen this cell-network hypothesis, we continue with large-scale numerical simulations.

4. Computational simulation of multiple cell samples

4.1. Outline of the approach

Direct computational experiments are achieved by solving Maxwell's equations numerically over samples of cells. This type of calculation has been performed for other general thermally-coupled electromagnetic heterogeneous media in Zohdi [25], and we follow a simplified version of that approach presently. In order to achieve this, we utilize a mathematical representation of the nominal bi-concaval RBC shape (Figs. 3 and 4)

$$F \stackrel{\text{def}}{=} \left(\frac{2(z-z_o)}{b}\right)^2 - \left(1 - \frac{(x-x_o)^2+(y-y_o)^2}{b^2}\right) \times \left(c_o + c_1\left(\frac{(x-x_o)^2+(y-y_o)^2}{b^2}\right) + c_2\left(\frac{(x-x_o)^2+(y-y_o)^2}{b^2}\right)^2\right)^2 = 0, \tag{4.1}$$

where the geometrical parameters, c_o, c_1 and c_2 are found in the work of Evans and Fung [6] (for example, $c_o = 0.207161$, $c_1 = 2.002558$ and $c_2 = -1.122762$), and where b is the radius of the cells. One can use this parametrization, in conjunction with a finite-difference mesh or finite-element mesh to develop a representation of a group of cells. For the numerical experiments, the position and orientation of each cell in the sample was random and not touching any neighboring cells (Figs. 4 and 5). The classical random sequential addition (RSA) algorithm (for placing non-intersecting objects in a domain) was used to place nonoverlapping cells randomly into the domain of interest [20]. This algorithm was adequate for the volume fraction range of interest. However, if higher volume fractions are desired, more sophisticated algorithms, such as the well-known, equilibrium-based, Metropolis algorithm can be used, while for extremely high volume fractions, approaches based on particle flow and growth are preferable [19,12,2–4]. The random orientation of the cells was controlled by using a random angle in a standard rotational coordinate transformation of the axes in Eq. (4.1) after placement within the domain.

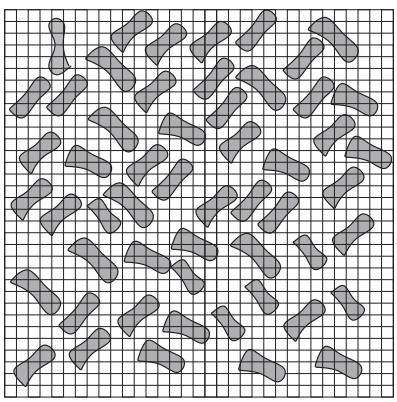

Fig. 4. A schematic of a mesh (actual meshes are much finer, see Fig. 5).

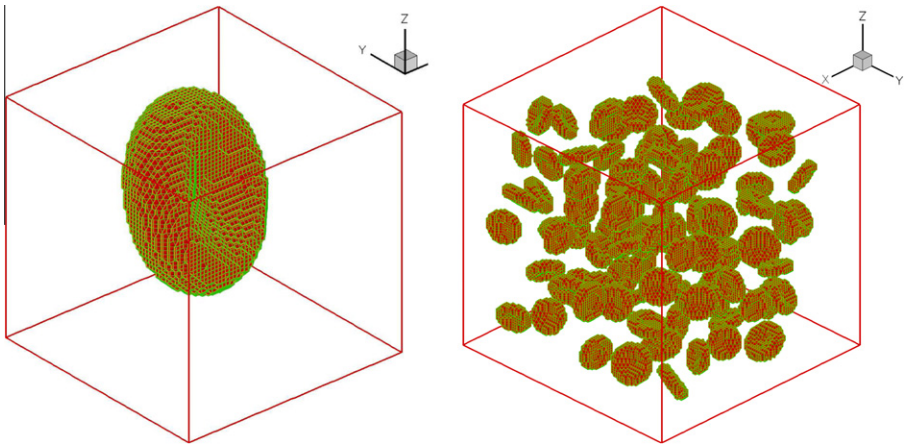

Fig. 5. Numerical (mesh) representation of a typical RBC (left) and a sample of blood at a volume fraction of $v_2 = 0.094$ (right). On the right is the resolution of the cell-system with a $101 \times 101 \times 101$ mesh which has 6181806 *electromagnetic degrees of freedom*. Approximately beyond the 61/81 mesh-density level there were no perceivable changes in the results.

4.2. Computational effective property calculation

We now develop a direct numerical scheme, based on the Finite Difference Time Domain (FDTD) Method to determine the electromagnetic response of a sample of blood by solving the coupled Maxwellian system (Faraday's law)

$$\nabla \times \boldsymbol{E} = -\frac{\partial(\boldsymbol{\mu} \cdot \boldsymbol{H})}{\partial t} \tag{4.2}$$

and (Ampere's law)

$$\nabla \times \boldsymbol{H} = \frac{\partial(\boldsymbol{\epsilon} \cdot \boldsymbol{E})}{\partial t}. \tag{4.3}$$

In order to perform volume averaging over an RVE, to obtain $\boldsymbol{\epsilon}^*$ computationally, we employ a "framing" technique, whereby uniform far-fields are applied on the boundary of a large sample, and the fields are averaged over an interior subsample, in order to avoid boundary layer effects, which occur from imposing the uniform fields on the larger sample exterior (Fig. 6). This is akin to exploiting a "St. Venant-type" decay effect, commonly exploited in solid mechanics, to avoid boundary layers. The approach provides a way of determining what the microstructure really experiences, without "bias" from the boundary loading. In order to determine $\boldsymbol{\epsilon}^*$(or any effective property), one specifies three uniform (spatially constant) linearly independent loadings of the form, for example either $\boldsymbol{E}$ or $\boldsymbol{D}$. Each of the loadings provides three linearly equations which can be used to solve for the nine constants in a general anisotropic effective permittivity tensor $\boldsymbol{\epsilon}^*$ (in reality there are only six constants, because $\boldsymbol{\epsilon}^*$ is symmetric). If the overall response is isotropic, which is the present case, since we have a mixture of randomly oriented cells, then only one test loading is needed, and the effective permittivity is given by Eq. (3.2). The practical implementation of "framing" is:

- *STEP (1)*: Generate a sample with a certain number of cells in its interior to meet the volume fraction under investigation,
- *STEP (2)*: For the effective property calculation (averaging), select a subsample ("a sub-box", Fig. 6) in the interior (to avoid boundary layer effects that arise from the imposition of uniform boundary conditions),

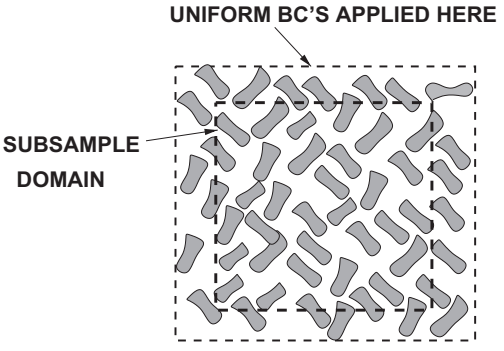

Fig. 6. A cell sample with uniform boundary fields applied to its exterior and an interior subsample for averaging purposes (to avoid boundary layer effects).

- *STEP (3)*: Repeat STEPS (1) and (2) for different random realizations for at a given sample sample size, and ensemble average the effective properties to determine a mean ($\boldsymbol{\epsilon}^*$) value,
- *STEP (4)*: Repeat STEPS (1)–(4) for a larger sample,
- *STEP (5)*: Continue the process (STEPS (1)–(4)) until the effective property ceases to change to within an acceptable tolerance.

The general discretization process follows an approach found in Zohdi [25], and is briefly outlined in the next section.
Remark. Similar relations holding for the magnetic permeability, relating the magnetic field flux (B) and the magnetic field (H), $\langle B\rangle_\Omega = \mu^* \cdot \langle H\rangle_\Omega$, and in the case of overall isotropy

$$\mu^* \stackrel{\text{def}}{=} \sqrt{\frac{\langle \boldsymbol{B}\rangle_\Omega \cdot \langle \boldsymbol{B}\rangle_\Omega}{\langle \boldsymbol{H}\rangle_\Omega \cdot \langle \boldsymbol{H}\rangle_\Omega}}. \tag{4.4}$$

4.3. Numerical discretization of Maxwell's equations

Following a general procedure found in Zohdi [26], let us now consider the direct numerical simulation of a blood sample by defining

$$\frac{\partial(\mu \boldsymbol{H})}{\partial t} = -\nabla_x \times \boldsymbol{E} \stackrel{\text{def}}{=} \boldsymbol{F} \quad \text{and} \quad \frac{\partial(\epsilon \boldsymbol{E})}{\partial t} = \nabla_x \times \boldsymbol{H} \stackrel{\text{def}}{=} \boldsymbol{G}. \tag{4.5}$$

We discretize for time = $t + \phi\Delta t$, and using a trapezoidal "$\phi - scheme$" ($0 \leqslant \phi \leqslant 1$)

$$\frac{(\mu \boldsymbol{H})(t+\Delta t) - (\mu \boldsymbol{H})(t)}{\Delta t} \approx \boldsymbol{F}(t+\phi\Delta t) \approx \phi \boldsymbol{F}(t+\Delta t) + (1-\phi)\boldsymbol{F}(t) \tag{4.6}$$

and

$$\frac{(\epsilon \boldsymbol{E})(t+\Delta t) - (\epsilon \boldsymbol{E})(t)}{\Delta t} \approx \boldsymbol{G}(t+\phi\Delta t) \approx \phi \boldsymbol{G}(t+\Delta t) + (1-\phi)\boldsymbol{G}(t). \tag{4.7}$$

Rearranging, yields

$$\boldsymbol{H}(t+\Delta t) \approx \frac{(\mu \boldsymbol{H})(t)}{\mu(t+\Delta t)} + \frac{\Delta t}{\mu(t+\Delta t)}(\phi \boldsymbol{F}(t+\Delta t) + (1-\phi)\boldsymbol{F}(t)) \tag{4.8}$$

and

$$\boldsymbol{E}(t+\Delta t) \approx \frac{(\epsilon \boldsymbol{E})(t)}{\epsilon(t+\Delta t)} + \frac{\Delta t}{\epsilon(t+\Delta t)}(\phi \boldsymbol{G}(t+\Delta t) + (1-\phi)\boldsymbol{G}(t)). \tag{4.9}$$

Numerically, the components of the curl of functions such as $\boldsymbol{E}$ are approximated by central finite-difference stencils of the form (Fig. 4):

$$\frac{\partial \boldsymbol{E}(x)}{\partial x} \approx \frac{\boldsymbol{E}(x+\Delta x) - \boldsymbol{E}(x-\Delta x)}{2\Delta x}, \text{ etc.} \tag{4.10}$$

In order to construct a solution, the algorithm is as follows:

(1) *Spatio-temporal discretization*: Construct spatial derivative terms such as

$$\frac{\partial \boldsymbol{E}(x)}{\partial x} \approx \frac{\boldsymbol{E}(x+\Delta x) - \boldsymbol{E}(x-\Delta x)}{2\Delta x}, \tag{4.11}$$

for each node (i,j,k), in conjunction with time-discretizations in Eqs. (4.8) and (4.9), leading to coupled systems abstractly written as

$$\boldsymbol{H}^{t+\Delta t} = \mathcal{F}(\boldsymbol{E}^{t+\Delta t}, \boldsymbol{H}^{t+\Delta t}) \quad \text{and} \quad \boldsymbol{E}^{t+\Delta t} = \mathcal{G}(\boldsymbol{E}^{t+\Delta t}, \boldsymbol{H}^{t+\Delta t}). \tag{4.12}$$

(2) *Staggered solution*: Compute $\boldsymbol{E}$-field with $\boldsymbol{H}$ fixed, then compute $\boldsymbol{H}$-field with $\boldsymbol{E}$ fixed, and iterate, $K = 1,2\ldots$ for

$$\boldsymbol{H}^{t+\Delta t,K} = \mathcal{F}(\boldsymbol{E}^{t+\Delta t,K}, \boldsymbol{H}^{t+\Delta t,K-1}) \text{ and } \boldsymbol{E}^{t+\Delta t,K} = \mathcal{G}(\boldsymbol{E}^{t+\Delta t,K-1}, \boldsymbol{H}^{t+\Delta t,K-1}). \tag{4.13}$$

(3) *Staggering error check:* Compute error measures: $\varpi_K^* \stackrel{\text{def}}{=} \max(\varpi_{E-K}, \varpi_{H-K}), i = 1, \ldots, nodes$

$$\varpi_{K-E} \stackrel{\text{def}}{=} \frac{\sum_{i=1}^N \|\boldsymbol{E}_i^{L+1,K} - \boldsymbol{E}_i^{L+1,K-1}\|}{\sum_{i=1}^N \|\boldsymbol{E}_i^{L+1,K} - \boldsymbol{E}_i^{L}\|}, \quad \varpi_{K-H} \stackrel{\text{def}}{=} \frac{\sum_{i=1}^N \|\boldsymbol{H}_i^{L+1,K} - \boldsymbol{H}_i^{L+1,K-1}\|}{\sum_{i=1}^N \|\boldsymbol{H}_i^{L+1,K} - \boldsymbol{H}_i^{L}\|}. \tag{4.14}$$

(4) *Updates*: When the tolerance is met, $\varpi^* \leqslant C_{tol}$ then increment time forward: $t = t + \Delta t$.

Remark. The time-step size used in the upcoming simulations allowed the algorithm to easily converge within a few iterations at each time-step. However, for more strongly-coupled systems, temporal (time-step) adaptivity is usually needed. Implicit, iterative procedures, with time-step adaptivity, are ideal for strongly-coupled thermo-electromagnetic and nonlinear systems (see [25]).

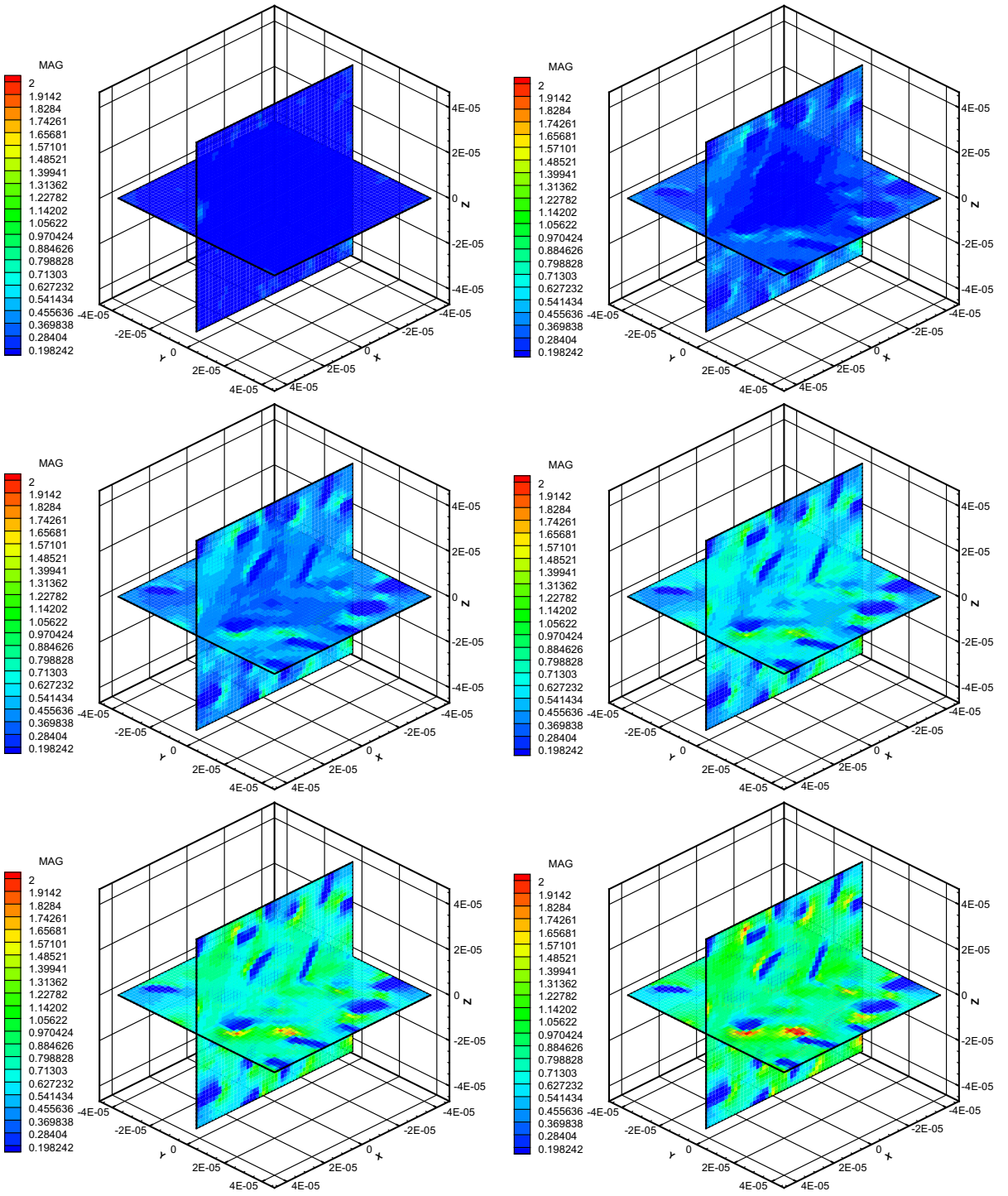

Fig. 7. Starting from left to right and top to bottom, the progressive evolution of the (normalized) electrical field $\frac{\|\boldsymbol{E}\|}{\|\boldsymbol{E}|_{\partial\Omega}(t=T)\|}$ magnitude within an 0.8-probe subsample (20% into the interior). $\boldsymbol{E}|_{\partial\Omega} = (10^9, 10^9, 10^9)\frac{t}{T}$, is the field applied on the exterior surface of the sample of blood at a volume fraction of $v_2 = 0.094$.

4.4. A model problem

As a model problem, we considered a group of N_p randomly dispersed, well-separated. cells, of equal size, in a cubical domain of dimensions, $D \times D \times D$ ($0.80 \times D$, was selected as the length-scale of the subsample). This sample size (and hence the number of cells, with the volume fraction held constant) was successively enlarged until there were no significant changes in the overall system response ($\boldsymbol{\epsilon}^*$) for further enlargements. For a more in depth discussion on size-effect issues for this class of systems, see the works of Zohdi [22,23,25]. We found that a sample that contained approximately $N_p = 100$ cells (Fig. 5) was adequate, i.e. further sample enlargements produced negligible changes in the computed effective properties. The following system parameters were used: $\epsilon_o = 8.854 \times 10^{-12}$ f/m, $\mu_o = 4\pi \times 10^{-7}\text{Ns}^2/\text{C}^2$, the electric field on the boundary (linearly-growing), $\boldsymbol{E}|_\Omega = (10^9, 10^9, 10^9)\frac{t}{T}$, initial conditions, $\boldsymbol{E}(t=0) = (0,0,0)$, magnetic field on the boundary (linearly-growing) and $\boldsymbol{H}|_\Omega = (10^9, 10^9, 10^9)\sqrt{\frac{\mu_o}{\epsilon_o}}\frac{t}{T}$, initial conditions, $\boldsymbol{H}(t=0) = (0,0,0)$. The relative magnetic permeability was set to 1 for the cells, $\mu_{2r} = 1$ and for the matrix, $\mu_{1r} = 1$ (the magnetic heterogeneity (mismatch) is essentially negligible). The relative permittivity of the cells was approximately $\epsilon_2/\epsilon_0 = 6000$, while the buffer was $\epsilon_1/\epsilon_0 = 81.12$. The cell size and volume fraction were determined by a cell/sample size ratio, which was defined via a subvolume size $V \overset{\text{def}}{=} \frac{D\times D\times D}{N_p}$. As an example, we used a volume fraction of approximately $v_2 = 0.094$, which corresponded to cells with a length-scale of $\mathcal{L} = 0.375$, which is a non-dimensional ratio between the major cell radius (b) and the subvolume given by $\mathcal{L} \overset{\text{def}}{=} \frac{b}{V^{\frac{1}{3}}}$. The length-scale dimension of the sample was $D = 50$ μm (see Fig. 7).

The meshes were sequentially refined in the following manner: (I) a $41 \times 41 \times 41$ mesh which has 413526 *nodal electromagnetic unknowns*, (II) a $61 \times 61 \times 61$ mesh which has 1361886 *nodal electromagnetic unknowns*, (III) a $81 \times 81 \times 81$ mesh which has 3188646 *nodal electromagnetic unknowns* and (IV) a $101 \times 101 \times 101$ mesh which has 6181806 *nodal electromagnetic unknowns*. Approximately beyond the 61/81-level there were no perceivable changes in the results. In Fig. 8, the progressive evolution of the effective permittivity, ϵ^*, from direct numerical simulation, within an 0.8-probe subsample (20% into the interior). The steady state relative effective permittivity value for this well-separated system was approximately $\epsilon_r^* = \epsilon^*/\epsilon_o \approx 125$, as opposed to the measured value (for the same volume fraction) of approximately $\epsilon_r^* = \epsilon^*/\epsilon_o \approx 400$. Thus, a system of well-separated cells is incapable of producing the observed experimental results, again suggesting the hypothesis that the the real system possesses network of touching cells.

5. Discussion and concluding remarks

The goal of this communication was to develop estimates of the volume fraction (hematocrit) levels from a macroscopic electromagnetic measurement of the overall permittivity of the cell-in-solution mixture. The approach taken here was to develop bounds on the possible volume fraction level by inverting the classical Hashin–Shtrikman bounds [11] on the effective response of electromagnetic mixtures. The utility of the approach is that given the permittivities of the buffer (known), cell (known) and whole mixture (measured) one can determine the cell volume fraction and compare it to the nominal response of a healthy group of cells. The deviation of the electromagnetic properties can be used to characterize certain blood disorders (thalassemia).

It is important to note that the expressions in Eq. (3.5) are valid for any combination of known values, ϵ_1, ϵ_2 and ϵ^* to obtain bounds on cell volume fraction (v_2) not necessarily just those of RBC mixtures. Through correlation of our laboratory measurements and the analytical expressions (bounds), it is hypothesized that RBCs may form high-permittivity cell-net-

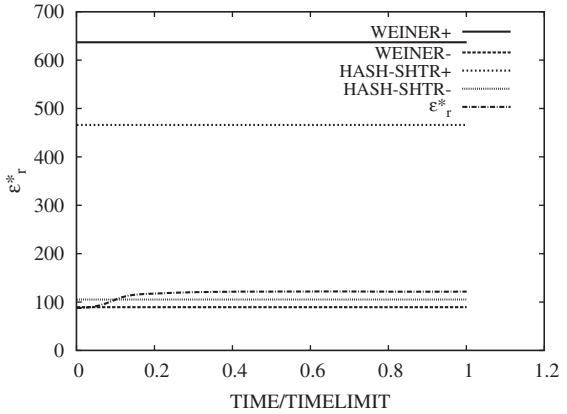

Fig. 8. The progressive evolution of the effective permittivity, ϵ^*, from direct numerical simulation, within an 0.8-probe subsample (20% into the interior). $\boldsymbol{E}|_\Omega = (10^9, 10^9, 10^9)\frac{t}{T}$, is the field applied on the exterior surface of the sample of blood at a volume fraction of $v_2 = 0.094$. The steady state value for this well-separated system was approximately $\epsilon_r^* \approx 125$, as opposed to the measured value (for the same volume fraction) of approximately $\epsilon_r^* \approx 400$, leading to the hypothesis that the real system must possess cell-network chains.

works by making cell-to-cell contact, even at low volume fraction. Furthermore, this work developed a computational electromagnetic technique, based on an implicit finite-difference discretization to solve the time-transient Maxwell's equations, in order to determine the response of samples of red blood cells, which was then used to indicate that it is impossible to generate the measured high overall (mixture) permittivities with well-separated cell morphologies. This again suggests the hypothesis that the cells may form networks, which is a subject of ongoing investigation by the authors.

References

[1] M. Bessis, Corpuscules, Springer-Verlag, Berlin, Heidelberg, New York, 1974.
[2] A. Donev, I. Cisse, D. Sachs, E.A. Variano, F. Stillinger, R. Connelly, S. Torquato, P. Chaikin, Improving the density of jammed disordered packings using ellipsoids, Science 303 (2004) 990–993.
[3] A. Donev, S. Torquato, F. Stillinger, Neighbor list collision-driven molecular dynamics simulation for nonspherical hard particles – I. Algorithmic details, Journal of Computational Physics 202 (2005) 737.
[4] A. Donev, S. Torquato, F. Stillinger, Neighbor list collision-driven molecular dynamics simulation for nonspherical hard particles – II. Application to ellipses & ellipsoids, Journal of Computational Physics 202 (2005) 765.
[5] S. Eber, S.E. Lux, Hereditary spherocytosis–defects in proteins that connect the membrane skeleton to the lipid bilayer, Seminars in Hematology 41 (2004) 118–141.
[6] E.A. Evans, Y.C. Fung, Improved measurements of the erythrocyte geometry, Microvascular Research 4 (1972) 335.
[7] B.G. Forget, A.R. Cohen, Thalassemia syndromes, in: B.E. Hoffman (Ed.), Hematology: Basic Principles and Practice, fourth ed., Elsevier, Philadelphia, 2005, pp. 557–558.
[8] P.G. Gallagher, Hereditary elliptocytosis: spectrin and protein 4.1R, Seminars in Hematology 41 (2004) 142–164.
[9] P.G. Gallagher, Update on the clinical spectrum and genetics of red blood cell membrane disorders, Current Hematology Reports 3 (2004) 5–91.
[10] Grant et al., A critical study of the open-ended coaxial line sensor technique for RF and microwave complex, Journal of Physics E: Scientific Instruments, 1989.
[11] Z. Hashin, S. Shtrikman, A variational approach to the theory of effective magnetic permeability of multiphase materials, Journal of Applied Physics 33 (10) (1962) 3125–3131.
[12] A. Kansaal, S. Torquato, F. Stillinger, Diversity of order & densities in jammed hard particle packings, Physical Review E 66 (2002) 041109.
[13] J.C. Maxwell, On the dynamical theory of gases, Philosophical Transactions Society of London 157 (1867) 49.
[14] J.C. Maxwell, A Treatise on Electricity and Magnetism, third ed., Clarendon Press, Oxford, 1873.
[15] J.W. Rayleigh, On the influence of obstacles arranged in rectangular order upon properties of a medium, Philosophical Magazine 32 (1892) 481–491.
[16] C. Schwan, Linear and nonlinear electrode polarization and biological materials, Annals of Biomedical Engineering, 1992.
[17] C. Schwan, Electrical properties of blood and its constituents: alternating current spectroscopy, Blut 46 (4) (1983) 185–197.
[18] M.H. Steinberg, E.J. Benz Jr., H.A. Adewoye, B.E. Hoffman, Pathobiology of the human erythrocyte and it's hemoglobins, in: B.E. Hoffman (Ed.), Hematology: Basic Principles and Practice, forth ed., Elsevier, Philadelphia, 2005, pp. 442–452.
[19] S. Torquato, Random Heterogeneous Materials: Microstructure and Macroscopic Properties, Springer-Verlag, New York, 2002.
[20] B. Widom, Random sequential addition of hard spheres to a volume, Journal of Chemical Physics 44 (1966) 3888–3894.
[21] O. Wiener, Zur Theorie der Refraktionskonstanten. Berichteüber die Verhandlungen der Königlich-Sächsischen Gesellschaft der Wissenshaften zu Leipzig, vol. Math.-phys Klasses, Band 62, 1910, pp 256–277.
[22] T.I. Zohdi, Genetic design of solids possessing a random-particulate microstructure, Philosophical Transactions of the Royal Society: Mathematical, Physical and Engineering Sciences 361 (1806) (2003) 1021–1043.
[23] T.I. Zohdi, P. Wriggers, Introduction to Computational Micromechanics, second ed., Springer-Verlag, 2008.
[24] T.I. Zohdi, F.A. Kuypers, Modeling and rapid simulation of multiple red blood cell light scattering, Proceedings of the Royal Society Interface 3 (11) (2006) 823–831.
[25] T.I. Zohdi, On the computation of the coupled thermo-electromagnetic response of continua with particulate microstructure, The International Journal of Numerical Methods in Engineering 76 (2008) 1250–1279.